Spontaneous switching of permeability changes in a limestone fracture with net dissolution

Amir Polak,[1,2] Derek Elsworth,[1] Jishan Liu,[3] and Abraham S. Grader[1]

[1] Results are reported for water flow-through experiments conducted on an artificial fracture in limestone at room temperature and under ambient confining stress of 3.5 MPa. Tests are concurrently monitored for mineral mass loss or gain and for changes in differential pressure between the inlet and outlet, throughout the 1500-hour duration of the experiment. Periodic imaging by X-ray computed tomography augments the fluid and mineral mass balance data and provides a third independent constraint on dissolution processes. The sample is sequentially circulated by water of two different compositions through the 1500-hour duration of the experiment, the first 935 hours by sampled groundwater (pH $\approx$ 8), followed by 555 hours of distilled water (pH $\approx$ 6). Large changes in the differential pressure are recorded throughout the experiment, for the constant flow rate of 2 cm^2/m; these are used as a proxy for recorded changes in fracture permeability, under invariant effective stress conditions. Mass of Ca and Mg were net-removed throughout the experiment. During the initial circulation of groundwater, the differential pressure increased almost threefold and is interpreted as a net reduction in permeability as the contacting asperities across the fracture are removed and the fracture closes. With the circulation of distilled water, permeability initially reduced threefold and ultimately increased by 2 orders of magnitude as a "wormhole" developed in the sample. This spontaneous switch from net decrease in permeability to net increase occurred with no change in experimental conditions of flow rate or applied effective stress, and Ca was net dissolved throughout. This behavior is attributed to the evolving localization of mass removal, triggered as free-face dissolution outcompetes stress-mediated dissolution at the asperity contacts. *INDEX TERMS:* 5114 Physical Properties of Rocks: Permeability and porosity; 1829 Hydrology: Groundwater hydrology; 5139 Physical Properties of Rocks: Transport properties; 8010 Structural Geology: Fractures and faults; *KEYWORDS:* fracture permeability, dissolution, precipitation, geochemistry, channeling

1. Introduction

[2] The natural development of karst, the purposeful acidization of carbonate petroleum reservoirs, and the proposed high-volume injection and recovery of surface waters via wells in the Florida Everglades are three prominent examples where nonequilibrium chemical and mechanical processes will drive changes in system porosity. The processes of dissolution and precipitation in porous media exert considerable influence in groundwater hydrology [*White*, 2002], groundwater chemistry [*Lasaga*, 1984], the enhancement of oil and gas production from petroleum reservoirs [e.g., *Hoefner and Fogler*, 1988; *Rege and Fogler*, 1989], changes in hydraulic conductivity as a result of mineral precipitation [e.g., *Tenthorey et al.*, 1998; *Aharonov et al.*, 1998], and in fluid flow through dissolution channels with connection to the Earth mantle [*Kelemen et al.*, 1995]. These processes may transfer large quantities of mass between the fluid and the solid mineral phases [*Domenico and Schwartz*, 1998].

[3] Changes in effective stresses, driven by injection and dewatering, and changes in reactive chemistry, driven by nonequilibrium chemical potentials, drive changes in porosity. For fractures as analogs of the flow system, the evolution in porosity is modulated by initial distributions of fracture aperture, and evolves in an apparently unpredictable manner as a function of the paths of stress, and of chemical potential, followed by the system. Importantly, for carbonate systems, close to equilibrium, the evolution of permeability is not single-sensed (see Figure 5b), and where stress paths are involved, fractures may either gape or close with net dissolution; permeability may increase as fast-flow channels are etched or may decrease as dissolution from bridging asperities brings fracture walls closer together.

[4] The competition between flow channel formation due to dissolution and channel destruction by precipitation [*Rege and Fogler*, 1989; *Singurindy and Berkowitz*, 2003]

---
[1]Energy Institute and Department of Energy and Geo-Environmental Engineering, Pennsylvania State University, University Park, Pennsylvania, USA.

[2]Now at Department of Civil and Environmental Engineering, Technion-Israel Institute of Technology, Haifa, Israel.

[3]School of Oil and Gas Engineering, University of Western Australia, Nedlands, Western Australia, Australia.
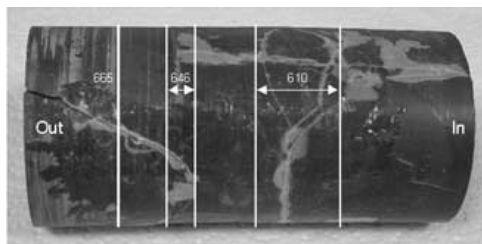
Figure 1. The limestone sample with its nonconnecting fractures and scanning areas.

illustrates the important roles of chemistry and flow rates in defining the potential for wormhole formation in carbonate rocks. The limited studies on fractures [*Durham et al.*, 2001; *Lin et al.*, 1997; *Moore et al.*, 1994; *Morrow et al.*, 2001] suggest an increased sensitivity of their transport properties to stresses and reactive chemical processes, over porous medium flows.

[5] This study examines the processes of dissolution and precipitation that progress within an induced fracture in limestone, specifically examining the evolution in permeability that develops under net dissolution as driven by changes in composition of the inlet solute. Detailed measurements of the driving fluid pressure, effective stresses, flow rates, influent and effluent fluid compositions, and the imaged interior structure of the fracture provide constraint to important processes controlling dissolution and precipitation.

2. Method

[6] The flow experiment was conducted on a cylindrical core (50 mm diameter × 108 mm length) of Bellefonte limestone containing a single diametral fracture intersecting an axial fracture as shown in Figure 1. The core was confined within a Viton® sleeve with end-to-end flow tests conducted within an industrial X-ray computed tomography (CT) scanner. For the applied steady flux, measured axial pressure differential yields a continuous record of the permeability constrained by intermittent X-ray scans.

2.1. Experimental Apparatus

2.1.1. The Coreholder and Flow System

[7] The fluid flow system and the coreholder are shown in Figure 2. The core holder is an 80-cm-long triaxial pressure cell of 9.5-cm outside diameter made of carbon fiber-reinforced aluminum tube (Temco Inc.) with stainless steel end plugs that are pierced by fluid supply tubes. Controlled flow rates and regulation of the confining pressure were prescribed by twin opposing-stroke Quizix (5400) pumps with an applied flow rate of 2 cm^2/min during the entire length of the experiment. The sample is sequentially circulated by water of two different compositions through the 1500-hour duration of the experiment, the first 935 hours by sampled groundwater, followed by 555 hours of distilled water, with an estimated residence time of the order of tens of seconds. The inlet water was pumped from a 6-L reservoir during both parts of the experiment.

2.1.2. The CT System

[8] X-ray imaging of two-dimensional slices perpendicular to the core axis was completed by a custom-made

industrial scanner (Universal systems, Inc.). The scanner produces two-dimensional slices through the sample with a thickness of 50 μm and an in-plane pixel resolution of 47 μm. The X-ray energy level used in the experiment was 195 kV at 800 μA. The core holder was removed from the CT scanner after each scanning procedure. In order to ensure proper registration of the CT images, two small (~1 × 1 × 1 mm) stainless steel targets were inserted into the outer flank of the fracture to act as fiducial marks. In each scanning sequence the CT system rotated the sample 360° while generating X rays that are detected by a digital camera that acts as a target. In each rotation the CT system takes 41 horizontal slices from the sample. Detailed descriptions on the use and limitations of X-ray CT in core analysis are given by *Stock* [1999], *Ketcham and Carlson* [2001], and *Wildenschild et al.* [2002].

2.2. Experimental Procedure

2.2.1. Core Packing and Vacuum Saturation

[9] After coring, the core sample was fractured using a Brazilian-like test [*Vukuturi et al.*, 1974] to produce a longitudinal plane fracture. The sample exterior was sealed with epoxy resin to prevent flow short-circuiting, sealed within a Viton® sleeve, and inserted into the core holder with hydraulic access via end-plugs. The confining fluid was added and pressured to 3.5 MPa, and the sample was evacuated to a pressure of 9 Pa for 24 hours. The experiment was initiated by vacuum saturation with water.

2.2.2. Scanning Procedure

[10] Following core packing, a total of four scans were taken at different stages of the experiment. All scanned sections are perpendicular to the core axis. A single rotation collects 41 slices, each of a thickness of ~50 μm. Successive rotations are completed by translating the sample relative to the static X-ray source and detector, enabling the scanning of larger volumes of the core. The first scan was carried out after saturation to determine whether the fracture was completely open throughout its length and to serve as a baseline for the rest of the experiment. Three scans followed, all at an effective stress of 3.5 MPa, and represented progress of the experiment at 938, 1173, and 1492 hours from the start of the experiment. Each scan
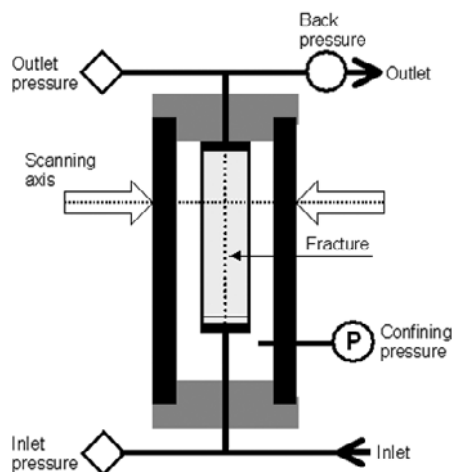
Figure 2. A schematic description of the experimental setup.

sampled volumes at three different axial locations in the core (610, 646, and 665, representing distances of 30, 66, and 85 mm, respectively, from the core inlet). The first location (610) had nine scanning rotations each of 41 slices, representing an axial length of 18.45 mm (50 μm for each slice). The second location (646) had three rotations, each of 41 slices, representing an axial length of 6.15 mm, and the third location had a single rotation with an axial length of 2.05 mm.

2.3. Experimental Analysis

[11] Concurrent X-ray imaging, indirect monitoring of the evolution of hydraulic aperture (via differential pressure measurement), and monitoring of solute mass, were completed.

2.3.1. Chemical Analysis

[12] During the 1500 hours of the experiment, 73 water samples were collected for chemical analysis of Al, Ba, Ca, Fe, K, Mg, Mn, Na, P, Si, and Sr using an inductively coupled plasma-atomic emission spectrophotometer with an estimated relative error of ±5%. Fourteen samples were collected from the inlet side and 59 were collected from the outlet side. The sample solutions were also analyzed for their pH values using a ROSS combination pH electrode (Thermo Orion).

[13] X-ray diffraction of the sample was performed using a Rigaku Geigerflex system with Cu radiation. The results show a strong calcite peak at $d = 3.03$ Å, with a much smaller dolomite peak at $d = 2.89$ Å. No magnesite was detected in the sample.

[14] In order to check the ratio between calcium and magnesium in the rock sample, three powder-crushed samples were weighed and immersed into 5% HNO_3 (1:1000 solid/liquid ratio) for 24 hours, to allow full dissolution of the solid phase. The samples were then analyzed by ICP for the ion concentrations. The results from this batch test show that only 8% of the sample is magnesium, by weight, and the rest is calcium. Fe, Na, Sr, Si, and K were also detected in the samples but with concentrations of less then 0.5 ppm. The presence of these ions is attributed to the small amount of clays that was found in the sample residue.

2.3.2. Fracture Aperture Analysis

[15] Differential pressure between the sample inlet and outlet were recorded throughout the duration of the flow-through tests with a resolution of ±40 Pa. Labview recorded two Quartzdyn QS transducers at six cycles/min. The low porosity of the limestone matrix enabled flow rates to be converted directly to equivalent hydraulic aperture via the parallel plate approximation [e.g., *Witherspoon et al.*, 1980; *Silliman*, 1989; *Piggott and Elsworth*, 1993]

$$Q = \frac{\Delta P}{12\mu L} b^3 W \qquad (1)$$

where μ is temperature-dependent dynamic viscosity of the fluid [M L^{-1} T^{-1}], L is length of the sample [L], W is diameter of the sample [L], Q is flow rate [L^3 T^{-1}], ΔP is the differential pressure [M T^{-2} L^{-1}], and b is the hydraulic aperture of the fracture [L]. The aperture was calculated only during the first 1080 hours of the experiment; for the remainder of the experiment, the changes in the differential pressure are converted to an approximate equivalent fracture

aperture, as the evolving flow conduit was tubular rather than planar.

[16] Rates of aperture reduction, db/dt, recovered from recorded effluent concentrations, may be compared with those independently recovered from the hydraulic test. For dissolution from beneath the contact area between two fracture surfaces, of area A_c[L^2], the rate of fracture closure, db/dt [L T^{-1}], may be defined as [*Polak et al.*, 2003]

$$\frac{db}{dt} = \frac{Q}{A_c} \left[\frac{C_{CACO_3}}{\rho_{CACO_3}} + \frac{C_{CaMg(CO_3)_2}}{\rho_{CaMg(CO_3)_2}} \right] \qquad (2)$$

where Q is the volumetric flow rate [L^3 T^{-1}], C and ρ are the concentration and density [M L^{-3}] of $CaCO_3$ and $CaMg(CO_3)_2$ (the two components that were detected in the sample using the X-ray diffraction system) in the effluent, respectively, calculated from the concentration measurements of Ca and Mg. These calculations enable the change in aperture to be determined from effluent concentrations and measured flow rates.

2.3.3. CT Image Analysis

[17] The redistribution of mineral mass within the fracture was examined throughout the test by subtracting sequential thresholded CT images. Sequential CT image pairs were selected with prescribed threshold CT-number (1670 and 1600, for the third and fourth time sequences, respectively) representing the transition from solid to pore space. Pixel counts define the volumetric transition from rock to pore space within the sample and enable quantification of mineral mass redistribution. This procedure was preformed on 12 pairs from different areas along the core.

3. Results and Discussion

[18] Two distinct behaviors exist within the test. The first is net reduction in aperture in the initial test period, when asperities are net removed, and the confining stress closed the facture. This reduction in aperture accelerates as the circulating fluid is first switched to distilled water. The second is a net increase in permeability resulting from the widening of a single dominant solution channel, termed a "wormhole," apparent in the differential pressure record, and corroborated by imaging. Contrasting models are developed for these two situations.

[19] The ensemble balances of fluid flow and mineral mass efflux, and CT imaging provide independent measurements of the process effecting mineral redistribution within the sample. Fluid flows constrain hydraulic apertures unequivocally, and cumulative measurements of mineral mass removal may be converted to changes in mechanical aperture if contact areas are known or estimated and an appropriate model for permeability enhancement assumed. Similarly, imaging defines changes in fracture porosity if resolution is sufficiently high. In the following we link observations of fluid and mineral flux, and imaging, with a consistent view of dominant processes and sites of dissolution, summarized in Table 1.

3.1. Mineral Mass Balance

[20] The influent and effluent concentrations of Ca and Mg are shown in Figure 3. Only three ions were detected in the inlet and outlet samples: Ca, Mg, and Na. The absence

Table 1. Estimated Volumes of Mineral Removed Throughout the Test as Sourced From Asperities or From Free-Face Dissolution

		Estimate of Volume Removed (mm^3) and Source of Evaluation			
Permeant	Time, hours	Concentration (Net Efflux)	Thin Section	X-Ray CT	Hydraulic [Aperture Change, μm]
Groundwater	0–935	360 (±180)			35[a] [−6]
Distilled water	935–1100	23 (±3)			18[a] [−6]
Distilled water[b]	1100–1500	108 (±6)	220[c]	170[c]	170 (50 mm)[c] [+32]
					53[c] (10 mm)
					20[c] (2 mm)

[a]Sourced from asperities.

[b]Magnitudes of mass removed for hydraulic data are consistent with observed pressure drop and flow rates, and for flow slot widths of 50, 10, and 2 mm. Negative aperture changes denote closing.

[c]Sourced from free-face dissolution.

of Na in concentrations above 0.5 ppm in the batch experiment suggested its presence was introduced only through the influent fluid, and at relatively high concentrations (∼20 ppm).

[21] The chemical composition of the influent water was switched after the initial 935 hours of circulation. For the initial circulation of groundwater, in near-chemical equilibrium with the limestone (0–935 hours), the inlet and outlet water chemistry is similar. Ca concentrations are of the order 45 ppm, and Mg is of the order 20 ppm for the first stage, with minor variations resulting from a changing water source. For the second stage of the experiment (935–1490 hours), distilled water is circulated, with influent Ca and Mg concentrations under the detection limit. Effluent concentrations of Mg remain below 0.1 ppm, and Ca concentrations asymptote to 4 ppm. This sudden elimination of Mg raises the suspicion that the measured inlet and outlet concentrations of Mg were primarily as a result of the inlet ground water and that the interaction with the rock matrix played a minor role. Measurement error bars show that only in two parts of the first experiment (∼180 and 800 hours) is there a substantial difference between the inlet and outlet concentrations.

[22] The variations between the differential concentrations (inlet minus outlet) are shown in Figure 4, where the positive numbers indicate net precipitation within the sample. The first part of the experiment is characterized by concentration differences that reach 22 and 7 ppm for Ca and Mg, respectively, with precipitation of mass during the first 100 hours followed by short episodes thereafter. The main period of active dissolution occurs after 500 hours when large amounts of Ca are removed (Figure 4a), followed by the delayed removal of smaller amounts of Mg beginning at about 700 hours. Error bounds on these measurements are relatively large, and hence the timing and delay in removal of Mg may not be significant. Absolute magnitudes of concentrations are of the order of 50 ppm, and relative errors are of the order of ±5%, as measured on concentration magnitudes ∼50 ppm. These correspond to error magnitudes of ∼5 ppm on the differential concentrations between inlet and outlet (Figure 3) in the early test and ∼0.25 ppm in the late test. These error observations suggest that the early-test data represent little net mass removal, while dissolution in the later test is real. This is substantiated by the observation of only minor increases in pH as the fluid transits from inlet to outlet

(Figure 4c) in the early test and a larger and more coherent change in the later test period. However, the identification of two periods when significant mass redistribution may occur is clear (70–190 and 640–890 hours), and these will be used to evaluate the mineral volume removed from the system.

[23] Mass removal rate is evaluated from the product of volumetric flow rate and species concentration, to yield cumulative mass removed. These calculations produce 265 and 137 mg for Ca and Mg, respectively, during the first
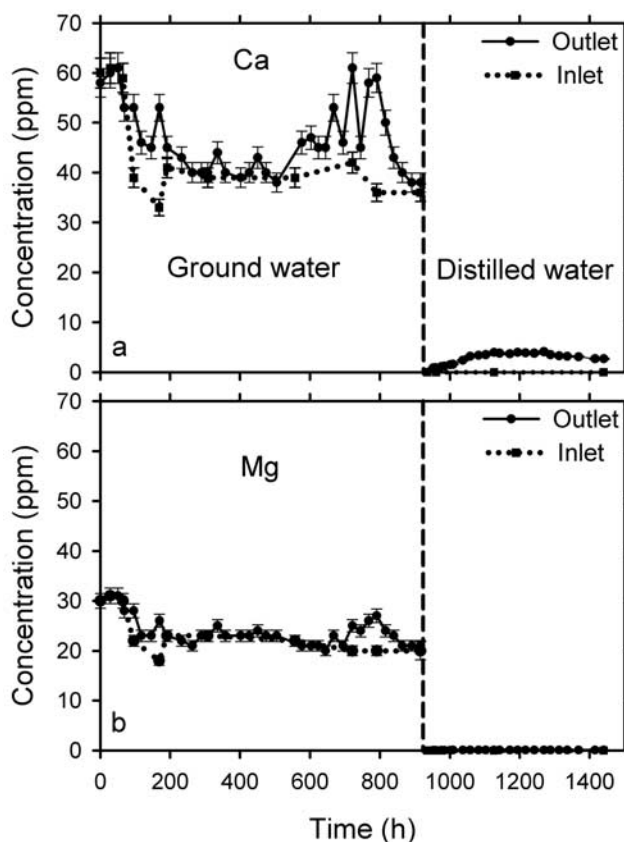
Figure 3. Chemical concentrations for the inlet and outlet samples for (a) Ca and (b) Mg. The vertical line at 935 hours signifies the change in the injected water chemistry, and the error bars were created for a relative error of 5%.
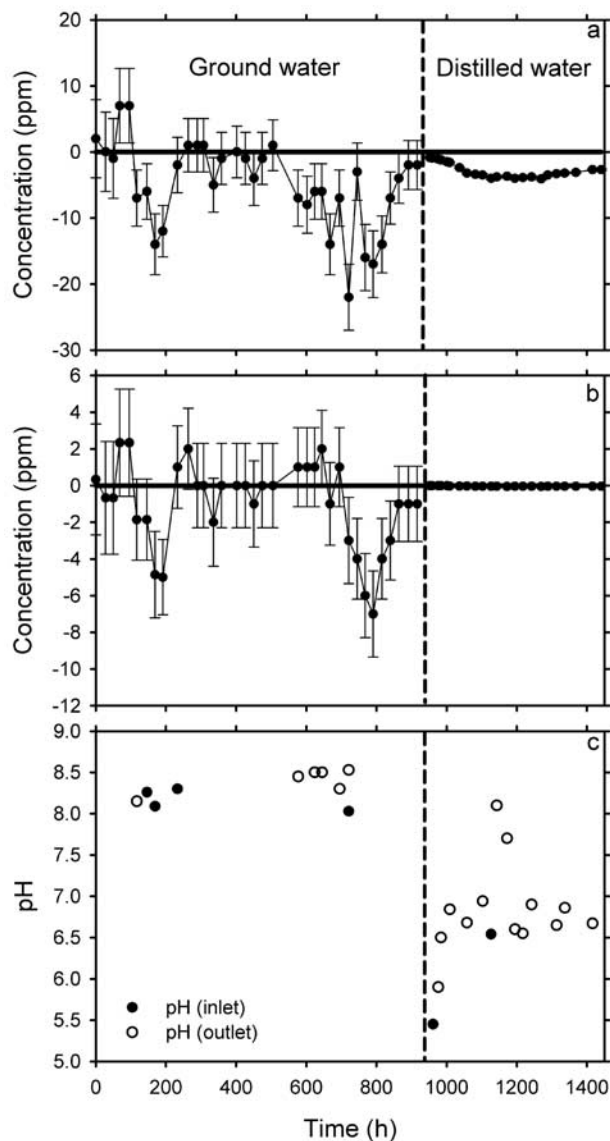
Figure 4. Concentration changes with time between the inlet and the outlet for (a) Ca and (b) Mg, at inlet and outlet. Positive values correspond to mass left in the fracture, and negative values correspond to mass taken out of the system. Note the large error bars that are the result of the combined error of each sample. (c) Change in measured pH magnitudes at inlet and outlet, with time.

part of the experiment. In order to calculate the mineral volume that was removed from the system, the mass of each ion was multiplied by the ratio of its origin mineral to give a corrected mass of 760 and 278 mg for $CaCO_3$ and $CaMg(CO_3)$, respectively (while Ca content was distributed 92% as $CaCO_3$ and 8% as $CaMg(CO_3)$). The total mineral volume that was removed from the system (using the density values of $CaCO_3$ and $CaMg(CO_3)$ as 2900 and 2840 kg/m^3, respectively) was 262 and 98 mm^3 for the first part of the experiment, bringing the total volume to 360 mm^3.

[24] During the second part of the experiment only Ca was detected in the effluent (Figures 3 and 4). The total measured mass of Ca was 189 mg, or 470 mg of $CaCO_3$,

representing a volume of 160 mm^3 and bringing the total mass removed to 520 mm^3.

[25] The solubility of calcium carbonate is affected by the pH of the solution [*Krauskopf and Bird*, 1995]. The overall process is represented by the reaction

$$CACO_3 + H_2CO_3 \Leftrightarrow Ca^{2+} + 2HCO_3^- \qquad (3)$$
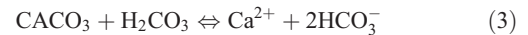
The rate of dissolution of calcite is not pH-dependent above pH 5.5 [*Plummer et al.*, 1978]. However, the precipitation rate of calcite increases with increasing pH above 5.5; therefore the net rate of dissolution in expected to be less in the groundwater than in the distilled water. The pH values are shown in Figure 4c. The differences in the pH values between the two stages of the experiment are explained by the change in the inlet water. During the first stage of the experiment, the inlet groundwater had an average pH of 8.15 and the outlet water had pH values from 8.15 to 8.53. During the second stage of the experiment, the inlet (distilled) water had an average pH of 6 while the pH of the outlet water was in the range 6–7. Influent and effluent pH magnitudes differ little throughout the experiment, suggesting that the extent of reaction in the core was low enough that pH was little changed.

3.2. Fluid Flux

[26] Under constant injected flow rate, the differential pressure recorded between the inlet and the outlet acts as a direct indicator for change in hydraulic aperture of the fracture. Differential pressure magnitudes are in the range 500–10 kPa for the duration of the experiment, with transducer resolution of the order of ±80 Pa; these are well resolved. The change in differential pressure with progress of the test, and corresponding change in equivalent aperture magnitude, are illustrated in Figure 5a. In the first stage of the experiment (0–935 hours) the pressure differential across the sample rises from 67 to 172 kPa, representing hydraulic apertures reducing from 24 to 18 μm. Aperture reduces at a rate of 0.0125 μm per hour for the first 500 hours before asymptoting to a final aperture of 20 μm. A power failure that stopped the injection pumps for a few minutes at 600 hours initiated a sharp drop in the aperture at a rate of 0.015 μm per hour for 120 hours, but again asymptoting to an equilibrium aperture of 18 μm over the final 200 hours of the first test stage. This differential pressure record corresponds to an initial decrease in permeability of 1 order of magnitude, followed by a spontaneous increase of 2 orders of magnitude (Figure 5b). Permeabilities were still increasing at the time the test was terminated.

[27] The second stage of the test, initiating with the circulation of distilled water, comprises two distinct patterns in flow behavior. Initially, differential pressures jump from 84 to 520 kPa over a period of 139 hours, corresponding to a reduction in fracture aperture from 18 to 12 μm (Figure 5). Subsequently, with no change in the composition of the influent water, pressure drops sharply from 520 to 11 kPa in 400 hours, corresponding to a 100-fold increase in permeability and an approximately fourfold increase in equivalent hydraulic aperture to 43 μm. This occurs without a significant change in the mass removal rate (Figure 6). Aperture increases at a rate of 0.075 μm per hour over these final 200 hours. Independent of the interpretation of the recorded
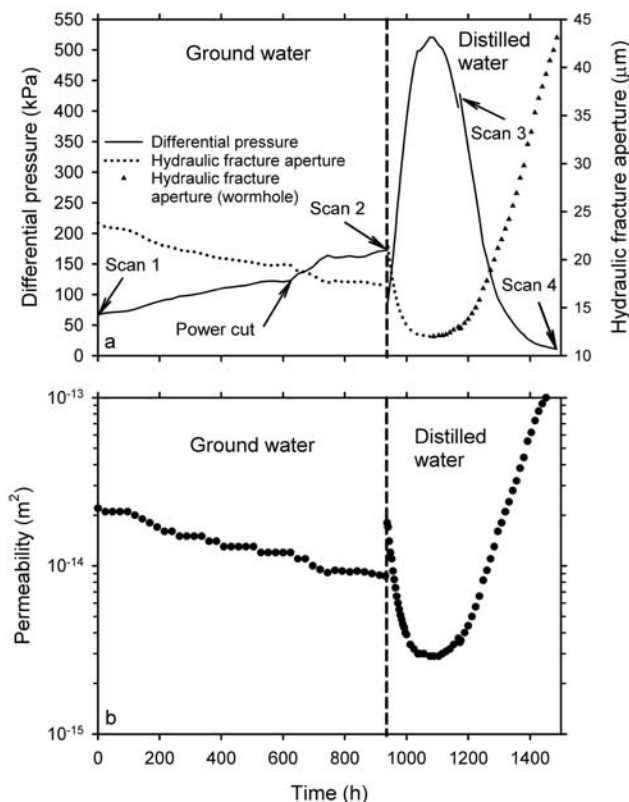
Figure 5. (a) Change in differential pressure (solid line) and corresponding hydraulic fracture aperture (dotted line) with time for continuous flow at 2 cm²/min through the fracture. Scanning sequences and the composition of injected water are noted. (b) Related change in permeability over the duration of the test.

differential pressures, the CT imaging indicates the development of a through-going wormhole, possibly invalidating this simple conceptualization as a parallel sided fracture.

3.3. CT Imaging

[28] The results of the first (0 hours) and fourth (1492 hours) scanning sequences at locations 610 and 665 (see Figure 1) are shown in Figures 7 and 8. The evolution of a wormhole is apparent in the time-lapse imaging sequence at location 665 (Figure 7), 85 mm downstream from the core inlet. Two horizontal fractures are visible, with the lower fracture noncontinuous out of the section plane; flow occurs in only the upper fracture. Changes in aperture are shown to localize on a narrow segment of the fracture that opens in response to net dissolution. An enlarged segment shows that even in the first scanning sequence the fracture appears closed, with an aperture lower than the spatial resolution of the CT imaging. At early time, the CT-number profile across the fracture shows a decrease in the CT numbers at the fracture (~2000) compared with the CT number of the matrix (~2200). As the fracture widens, the trough in the CT-number profile deepens from ~1800 to ~1300, as individual pixels fully register the signature of the water-filled void, rather than a mixed sample of void and matrix. This CT-number differential of ~500 may be used to calibrate for the presence and extent

of fracture voids. The absolute difference in the CT-numbers recorded for the matrix, in the two successive scans, is a calibration difference and does not indicate a change in any chemical or physical parameters of the sample.

[29] Two vertical fractures and one horizontal fracture are visible in the profile taken upstream of the prior section (Figure 8). Location 610 is 30 mm from the core inlet (Figure 1). The two vertical fractures are oblique to the section, and their apparent apertures are consequently enlarged over their true magnitude. These fractures are not hydraulically connected and extend only a few millimeters along the core axis, as apparent in adjacent scanned images. Consequently, these nonflowing fractures exhibit little change in apparent aperture in the time-lapse sequence of images shown in Figure 8. Conversely, time-lapse changes in aperture are apparent within the flowing horizontal fracture where a dissolution tube opens close to the core center, upstream of the feature observed at location 665. The CT-number profile shows a similar signature of the fracture to that observed downstream, where a trough of ~500 below a plateau of ~1800 enables the delineation of the evolving dissolution feature. This signature may be used both to delineate features that extend more than one pixel in size and to calibrate features at the subpixel level.

4. Process-Based Models for Permeability Change

[30] Two different behaviors are apparent during the test: Apertures first reduce, under presumed net dissolution, and then gape as net dissolution is more positively apparent. Net dissolution is confirmed throughout the test by two independent indicators: that inlet pH is always lower than outlet pH and that net efflux of mineral mass is recorded throughout. Mechanistic models are proposed to replicate these behaviors. These define permeability reduction as mineral mass is net removed from contacting asperities, and permeability enhancement as free-face dissolution localizes along a solution channel. If mineral matter is uniformly removed from either the face of the conducting fracture, or the bridging asperities, then measured effluent mass removal
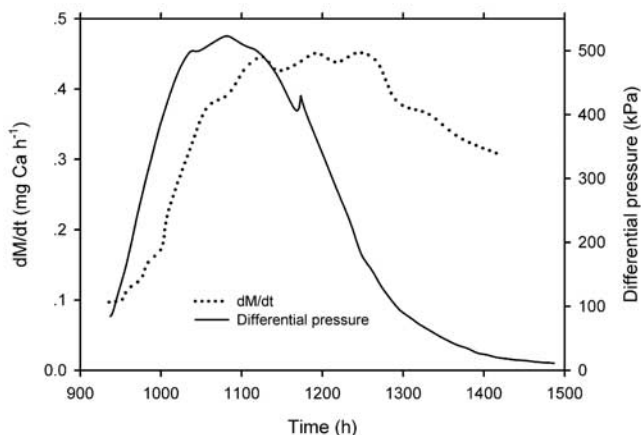
Figure 6. Change in mg of Ca per hour (*dM/dt*) (dotted line) and the corresponding differential pressure (solid line), with time during the second part of the experiment.
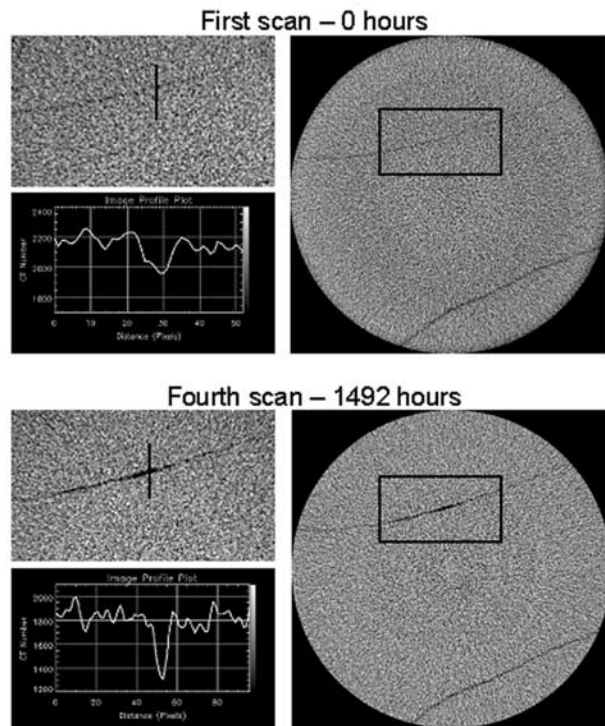
Figure 7. Scanned images for the core at longitudinal location 665, 85 mm downstream of the inlet, at (a) test initiation (0 hours), and (b) after 1492 hours.

monotonically increased. The subsequent rapid growth of permeability is attributed to the development of a single primary solution channel, with this feature apparent in the imaging data. This self-organized switch in behavior, from net permeability reduction to net increase, with no change in test conditions, is constrained in the following with the independent measurements of flow rate, mineral flux, and the scanning data.

4.2.1. Net Reduction in Permeability

[33] With the initial switch in permeant, an accelerating rate of permeability reduction correlates with a slowly increasing rate of net Ca removal (Figure 6). This increasing rate of mass removal is indexed by the rise of Ca concentrations from near background levels ($\sim$0.001 ppm) to a steady peak magnitude of 5 ppm, as apparent in Figure 4. The measured rate of mass removal correlates with the measured change in differential fluid pressure, as illustrated in Figure 6. Since flow rate remains constant throughout the test, a consistent model links accelerating dissolution from asperities as a feasible source of reduction in fracture permeability, represented by the proxy increase in driving pressure. The measured 23 mm^3 of mineral mass removed during the period 935–1100 hours correlates with a net reduction in fracture aperture of 8 μm if the contact area of the asperities is of the order 50% (equation (2)). This assumed fracture contact area is at the upper limit of those measured where hydrochemical effects are not apparent [e.g., *Pyrak-Nolte et al.*, 1987; *Zimmerman and Bodvarsson*, 1996; *Polak et al.*, 2003], but the evaluated

rates should scale directly with measured changes in fracture aperture.

4.1. Circulation of Groundwater: Net Dissolution and Permeability Reduction

[31] The 6.4-μm reduction in fracture aperture, measured during the first 935 hours of the test (Figure 5), represents a total volume of 35 mm^3 if distributed over the entire 5500-mm^2 (51 × 108 mm) surface area of the fracture. This represents a predicted upper bound on the volume removed from asperities, as contact area must be less than 100%. However, even this upper bound is an order of magnitude lower than the net volume evaluated from the chemical efflux data, of 360 mm^3. This suggests either that the material removed from the sample was drawn from a broader source than the asperities of a single fracture or that the contacting asperities and free-face surface of the fracture both participated in the dissolution. The resolution of the imaging is unable to definitively discriminate between these two scenarios, although the source volume for the excess dissolved mineral mass would be the non-connecting fractures visible in the scans of Figure 8, for example.
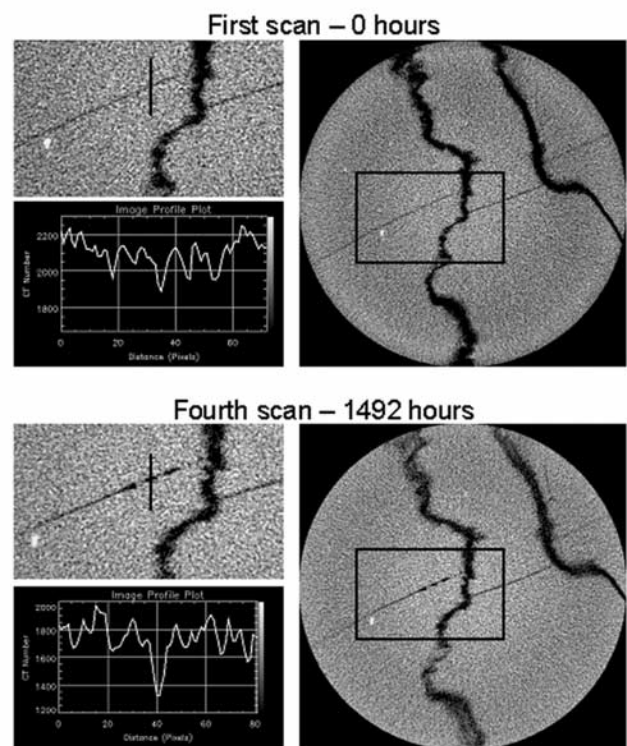
4.2. Circulation of Distilled Water: Net Dissolution and Spontaneous Permeability Switching

[32] The changes in permeability that occurred within the second portion of the test may be correlated with the growing and coherent net removal of mineral mass from the sample, as apparent following the initial circulation of distilled water at hour 932. With the introduction of the distilled water, permeability first dropped abruptly and then

Figure 8. Scanned images for the core at longitudinal location 610, 36 mm downstream of the inlet, at (a) test initiation (0 hours), and (b) after 1492 hours.
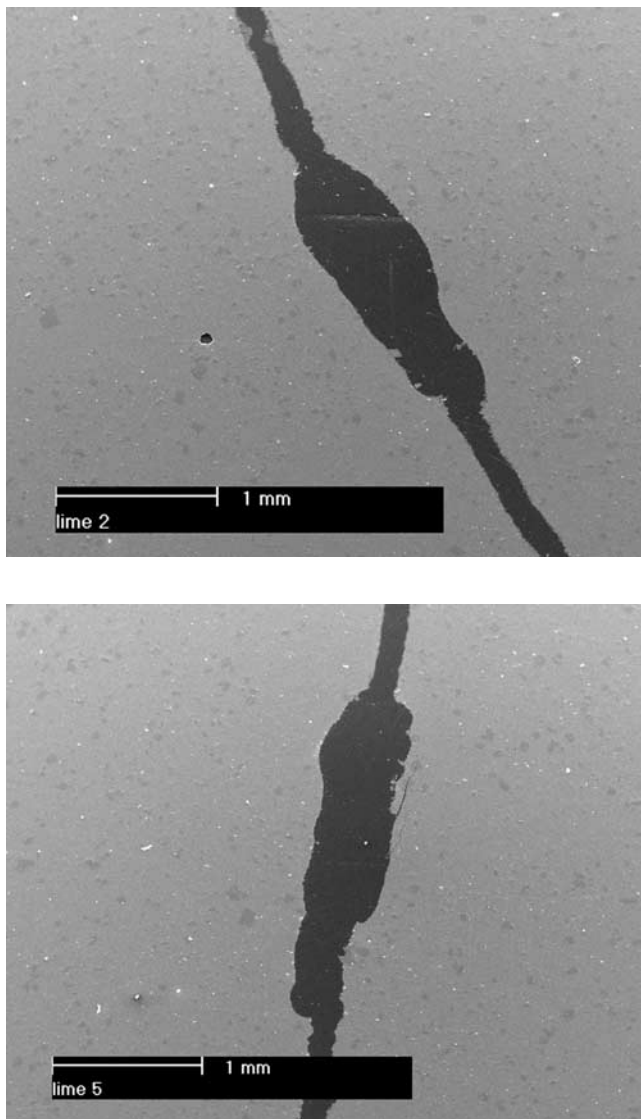
Figure 9. A thin-section image of a wormhole taken by SEM (magnified by 25) at two different locations approximately (a) 29 mm and (b) 46 mm from the core inlet.

8-μm reduction correlates closely with the 6-μm reduction in fracture aperture recovered from the hydraulic data.

4.2.2. Net Increase in Permeability

[34] Flow localization initiated after distilled water had been circulated within the fracture for 100 hours, as apparent in the differential pressure record, and continued for the following 300 hours. To constrain processes contributing to this behavior, we attempt to constrain the geometry of the evolving dissolution feature. The evolution of the wormhole may be constrained by four independent measurements: direct measurement of wormhole geometry from thin sections, nondestructive imaging by X-ray CT, and constraint placed by proxy measurements of pressure drop and net mineral loss from the sample, with progress of the test. Constraints placed by these four suites of independent measurements are compared.

4.2.2.1. Thin-Section Analysis

[35] A total of seven thin sections were taken perpendicular to the sample axis, and at distributed locations. Figure 9

shows two thin sections recovered approximately 29 and 46 mm downstream of the core inlet that contain a through-going fracture of approximately 150 μm in aperture, with an embedded central flow conduit. Notably, the observed mean fracture aperture of 150 μm is larger than that predicted from the hydraulic measurements (Figure 5) and is influenced by the sampling process; the unfused halves of the core were removed from the core holder at the conclusion of the test and have sustained displacements. Constraining the separation of the thin-section fracture walls to the hydraulically measured minimum aperture (12 μm, as apparent in Figure 5), then the two measured wormhole sections are of the order of 350 μm in aperture and 1800 μm in width. These are representative of the remaining five thin sections and account for a volume of 220 mm^3 when extended for a through-going conduit. This closely matches the 160 mm^3 of mass removal recorded from the mineral efflux data. The concave inward surfaces of the widened conduit are not apparent within the main portion of the fracture, indicating that the flow was concentrated on the widened portion of the conduit and explaining the declining Ca concentrations recorded in the late test following flow localization (Figure 3).

4.2.2.2. CT-Image Subtraction

[36] Conduit morphology and volume may be independently estimated by image subtraction for CT images taken both before (scan 3) and after the creation of the wormhole (scan 4). A total of 12 images were selected, representing 30% of the entire sample. The two sets of images are shown in Figure 10, at positions 36 and 84.5 mm from the core inlet. The binary pixel map is constructed for a threshold CT number of between 1600 and 1625 to represent the transition between rock and void. The threshold changes, depending on the calibration for each scan location. The upper pair of images (36 mm from the inlet) represents an area of 25 $\times$ 10 mm that straddles the fracture and the lower set (84.5 mm from the inlet) an area of 17 $\times$ 6 mm. The scattered pores of sequence 3 precede the evolution of the wormhole and represent total cross-sectional flow areas of 0.87 mm^2 (391 pixels) and 0.26 mm^2 (116 pixels) at the upstream and downstream locations, respectively. After the formation of the wormhole, some preexisting pores have disappeared, consistent with the observed reduction in permeability that directly followed the introduction of distilled water as the permeant. Subsequently, a wormhole has formed (sequence 4) from apparently unremarkable starter pores. The summed fracture areas evolve to 3.73 mm^2 (1733 pixels) and 0.79 mm^2 (366 pixels) for upstream and downstream locations. This represents a roughly fourfold increase in cavity sectional area and indicates the variable geometry of the conduit along its length. Repeating this procedure for the remaining 10 scan locations, and weighting the volumetric coverage from 30% to 100%, results in a total estimated wormhole volume of 170 mm^3.

4.2.2.3. Hydraulic Measurements

[37] The measured differential pressure may be used to estimate the average aperture of a high aspect-ratio slit, corresponding to the thin-section geometry of Figure 9. The observed change in pressure drop from 520 to 11 kPa corresponds to an increase in an equivalent aperture of 31 μm (increasing from an aperture of 12 μm at hour 1088 of the experiment). When extended across the full
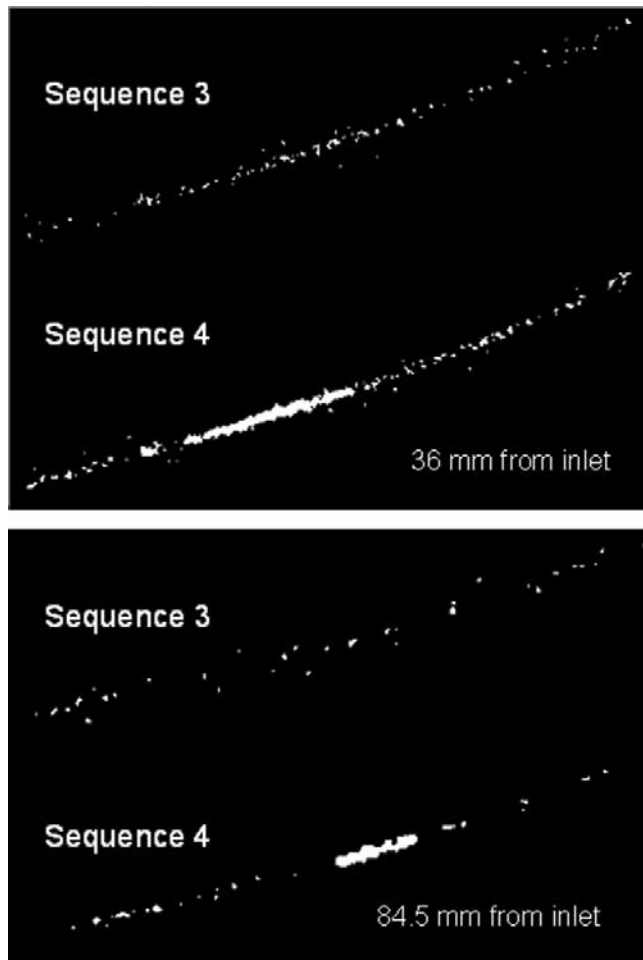
Figure 10. Two sets of CT images taken from two different locations, (a) 36 mm and (b) 84.5 mm from the core entrance. In each set of images the upper image is from the third (before the creation of the wormhole) scanning sequence and the lower image from the fourth (after the creation of the wormhole) scanning sequence. In each scanning sequence a threshold value was set to signify the transition between the matrix and the fracture.

sample, this represents an equivalent removed volume of 170 mm^3. Alternatively, for the approximately 2000 μm (2 mm) wide slot observed in thin section (Figure 9), the same pressure drop corresponds to an increase in aperture of 91 μm, representing a total volume removed of only 20 mm^3. A slot of 10 mm corresponds to an aperture change of 53 μm and a total volume removed of 53 mm^3.

4.2.2.4. Mineral Mass Removal

[38] Finally, measurements of the mineral mass removed following the switching of permeants may also constrain total changes in porosity. The total mass removed during the permeability-enhancement stage of the test is 300 mg of $CaCO_3$ (Ca was the only ion found during that time), representing a total volume of 108 mm^3. This volume is smaller than that estimated from the other approaches. Notably, the CT and the thin-section results are a direct measurement of the final wormhole size, while estimates from hydraulic measurements, and from cumulative mass removed, are indirect.

[39] Overall, these four complementary but independent approaches yield consistent estimates of the volume of the evolving solution feature, save the hydraulic estimates. The variable fracture aperture and the distribution of the contact area determine the shape and volume of the mass that will be removed in the dissolution process. The measurement of the differential pressure at the inlet and outlet sides of the fracture gives only an average magnitude of aperture, which does not reveal the true distribution along the entire flow path. By using the CT system we can, within the limitations of resolution, follow the heterogeneity of the fracture and its evolution in time.

5. Conclusions

[40] The results from this experimental study examine the controls exerted by dissolution and precipitation on flow inside an artificial fracture in limestone. Processes accompanying the continuous flow of water at ambient temperatures for 1500 hours are constrained by the continuous measurement of differential pressure and chemical concentration of the inflow and outflow, together with periodic imaging by X-ray CT. The flow of groundwater in the first part of the experiment caused the impedance to increase monotonically as contacting asperities are removed and the fracture walls close. Measured net mineral efflux magnitudes are an order of magnitude larger than those sensibly required to generate the measured change in impedance, if the source of the mass is the contacting asperities, alone. Correspondingly, the fractured interior of the sample must contribute to the measured mass removed, despite the significant errors attached to the measured net efflux.

[41] The switch in permeant from groundwater to distilled water caused accelerating changes in flow impedance; an initial rapid increase in impedance (closure in aperture), subsequently halted, and spontaneously transformed into an exponentially decreasing impedance, corresponding to the observed growth of a wormhole. The initial measured increase in impedance is consistent with closure of the fracture resulting from the fast removal of asperities from contact areas. This rapid increase in impedance correlates with a slow rise in effluent concentrations of Ca to an equilibrium magnitude of 5 ppm. The cumulative mineral volume removed during this stage (23 mm^3) corresponds closely with that predicted from the hydraulic data (23 mm^3), assuming a 50% contact area across the fracture walls. Stated differently, the hydraulically sampled reduction in fracture aperture of 6 μm corresponds closely with the 8-μm reduction evaluated from the mineral-mass efflux data, assuming a 50% fracture contact area.

[42] With continued circulation of distilled water at constant flow rate, the sample reaches a maximum impedance as the concentration of the effluent approaches a steady maximum of 5 ppm Ca. Following this, the impedance sharply drops with the observed development of a dominant flow channel. This occurs with no changes in the other experimental conditions, or in the resulting concentration of the effluent, recording net removal of mass in the sample. Estimates of cumulative mass removed, evaluated from the aqueous efflux data, correspond closely to estimates from destructive thin-section and nondestructive X-ray CT measurements. Estimates of conduit geometry from the

supporting hydraulic data are more ambiguous. Through-going conduits, the dimension of the observed wormholes, are considerably more conductive than the observed pressure drops suggest. Correspondingly, conduit volumes evaluated from the hydraulic data alone are much smaller than the consistent predictions from mineral efflux data and measured dimensions from thin sections and X-ray CT. Since consistent predictions exist between the ensemble suite of concentration, thin section, and X-ray CT data, these models suggest that flow constrictions along the length of the wormhole present large impedances that are not readily accommodated using aggregate conduit cross-sectional dimensions. In the absence of imaging data, it would not be possible to remove the ambiguity between the mass efflux data and the observed change in hydraulic impedance of the sample. This observed switching in permeability under net dissolution has implications in the rate of formation of karst and in potential changes in porosity and permeability that may accompany the injection and recovery of surface waters in the proposed restoration of the Florida Everglades. These observed changes in porosity affect the rates of channel evolution in fractures, their resulting morphology, and their consequences in developing fast flow pathways, depressed entry pressures, enhanced immiscible phase mobility, and suppressed mechanisms for retardation and attenuation of aqueous and particulate contaminants alike.

References

Aharonov, E., E. Tenthorey, and C. H. Scholz (1998), Precipitation sealing and diagenesis: 2. Theoretical analysis, *J. Geophys. Res.*, *103*(B10), 23,969–23,981.

Domenico, P. A., and F. W. Schwartz (1998), *Physical and Chemical Hydrogeology*, 2nd ed., John Wiley, Hoboken, N. J.

Durham, W. B., W. L. Bourcier, and E. A. Burton (2001), Direct observation of reactive flow in a single fracture, *Water Resour. Res.*, *37*(1), 1–12.

Hoefner, M. L., and H. S. Fogler (1988), Pore evolution and channel formation during flow and reaction in porous media, *AIChE J.*, *34*(1), 45–54.

Kelemen, P. B., J. A. Whitehead, E. Aharonov, and K. A. Jordahl (1995), Experiments on flow focusing in soluble porous media, with applications to melt extraction from the mantle, *J. Geophys. Res.*, *100*(B1), 475–496.

Ketcham, R. A., and W. D. Carlson (2001), Acquisition, optimization and interpretation of X-ray computed tomographic imagery: Applications to the geosciences, *Comput. Geosci.*, *27*, 381–400.

Krauskopf, K. B., and D. K. Bird (1995), *Introduction to Geochemistry*, McGraw-Hill, New York.

Lasaga, A. C. (1984), Chemical kinetics of water-rock interactions, *J. Geophys. Res.*, *89*(B6), 4009–4025.

Lin, W., J. Roberts, W. Glassley, and D. Ruddle (1997), Fracture and matrix permeability at elevated temperatures, paper presented at the Workshop on Significant Issues and Available Data: Near-Field/Altered-Zone Coupled Effects Expert Elicitation Project, Dep. of Energy, San Francisco, Calif., November .

Moore, D. E., D. A. Lockner, and J. A. Byerlee (1994), Reduction of permeability in granite at elevated temperatures, *Science*, *265*(5178), 1558–1560.

Morrow, C. A., D. E. Moore, and D. A. Lockner (2001), Permeability reduction in granite under hydrothermal conditions, *J. Geophys. Res.*, *106*(B12), 30,551–30,560.

Piggott, A. R., and D. Elsworth (1993), Laboratory assessment of the equivalent apertures of a rock fracture, *Geophys. Res. Lett.*, *20*(13), 1387–1390.

Plummer, N. L., T. M. L. Wigley, and D. L. Parkhurst (1978), The kinetics of calcite dissolution in CO_2-water systems at 5 to 60°C, and 0 to 1 atm CO_2, *Am J. Sci.*, *278*(2), 179–216.

Polak, A., D. Elsworth, H. Yasuhara, A. S. Grader, and P. M. Halleck (2003), Permeability reduction of a natural fracture under net dissolution by hydrothermal fluids, *Geophys. Res. Lett.*, *30*(20), 2020, doi:10.1029/2003GL017575.

Pyrak–Nolte, L. J., L. Myer, N. G. W. Cook, and P. A. Witherspoon (1987), Hydraulic and mechanical properties of natural fractures in low permeability rock, in *Proceedings of the International Congress for Rock Mechanics*, pp. 225–231, Int. Soc. for Rock Mech., Lisbon.

Rege, D. S., and H. S. Fogler (1989), Competition among flow, dissolution, and precipitation in porous media, *AIChE J.*, *35*(7), 1177–1185.

Silliman, S. E. (1989), An interpretation of the difference between aperture estimates derived from hydraulic and tracer tests in a single fracture, *Water Resour. Res.*, *25*(10), 2275–2283.

Singurindy, O., and B. Berkowitz (2003), Evaluation of hydraulic conductivity by precipitation and dissolution in carbonate rock, *Water Resour. Res.*, *39*(1), 1016, doi:10.1029/2001WR001055.

Stock, S. R. (1999), X-ray microtomography of materials, *Int. Mater. Rev.*, *44*(4), 141–164.

Tenthorey, E., C. H. Scholz, and E. Aharonov (1998), Precipitation sealing and diagenesis: 1. Experimental results, *J. Geophys. Res.*, *103*(B10), 23,951–23,967.

Vukuturi, V. S., R. D. Lama, and S. S. Saluja (1974), *Handbook on Mechanics Properties of Rocks*, vol. 1, Trans Tech Publ., Enfield, N. H.

White, W. B. (2002), Karst hydrology: Recent developments and open questions, *Eng. Geol.*, *65*, 85–105.

Wildenschild, D., J. W. Hopmans, C. M. P. Vaz, M. L. Rivers, D. Rikard, and B. S. B. Christensen (2002), Using X-ray computed tomography in hydrology: Systems, resolutions, and limitatations, *J. Hydrol.*, *267*, 285–297.

Witherspoon, P. A., J. S. Y. Wang, K. Iwai, and J. E. Gale (1980), Validity of cubic law for fluid flow in a deformable rock fracture, *Water Resour. Res.*, *16*(6), 1016–1024.

Zimmerman, R. W., and G. S. Bodvarsson (1996), Hydraulic conductivity of rock fractures, *Transp. Porous Media*, *23*(1), 1–30.

————————————

D. Elsworth and A. S. Grader, Energy Institute and Department of Energy and Geo-Environmental Engineering, Pennsylvania State University, 403 Academic Activities Building, University Park, PA 16802, USA. (elsworth@psu.edu)

J. Liu, School of Oil and Gas Engineering, University of Western Australia, 35 Stirling Highway, Western Australia 6009, Australia.

A. Polak, Department of Civil and Environmental Engineering, Technion-Israel Institute of Technology, Haifa 32000, Israel.